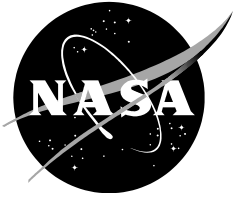


NASA/TM-2016-219154



Flat Plate Wake Velocity Statistics Obtained with Circular and Elliptic Trailing Edges

*Man Mohan Rai
Ames Research Center
Moffett Field, CA-94035*

August 2016

NASA STI Program ... in Profile

Since its founding, NASA has been dedicated to the advancement of aeronautics and space science. The NASA scientific and technical information (STI) program plays a key part in helping NASA maintain this important role.

The NASA STI program operates under the auspices of the Agency Chief Information Officer. It collects, organizes, provides for archiving, and disseminates NASA's STI. The NASA STI program provides access to the NTRS Registered and its public interface, the NASA Technical Reports Server, thus providing one of the largest collections of aeronautical and space science STI in the world. Results are published in both non-NASA channels and by NASA in the NASA STI Report Series, which includes the following report types:

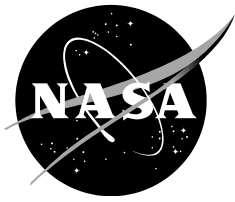
- **TECHNICAL PUBLICATION.** Reports of completed research or a major significant phase of research that present the results of NASA Programs and include extensive data or theoretical analysis. Includes compilations of significant scientific and technical data and information deemed to be of continuing reference value. NASA counterpart of peer-reviewed formal professional papers but has less stringent limitations on manuscript length and extent of graphic presentations.
- **TECHNICAL MEMORANDUM.** Scientific and technical findings that are preliminary or of specialized interest, e.g., quick release reports, working papers, and bibliographies that contain minimal annotation. Does not contain extensive analysis.
- **CONTRACTOR REPORT.** Scientific and technical findings by NASA-sponsored contractors and grantees.
- **CONFERENCE PUBLICATION.** Collected papers from scientific and technical conferences, symposia, seminars, or other meetings sponsored or co-sponsored by NASA.
- **SPECIAL PUBLICATION.** Scientific, technical, or historical information from NASA programs, projects, and missions, often concerned with subjects having substantial public interest.
- **TECHNICAL TRANSLATION.** English-language translations of foreign scientific and technical material pertinent to NASA's mission.

Specialized services also include organizing and publishing research results, distributing specialized research announcements and feeds, providing information desk and personal search support, and enabling data exchange services.

For more information about the NASA STI program, see the following:

- Access the NASA STI program home page at <http://www.sti.nasa.gov>
- E-mail your question to help@sti.nasa.gov
- Phone the NASA STI Information Desk at 757-864-9658
- Write to:
NASA STI Information Desk
Mail Stop 148
NASA Langley Research Center
Hampton, VA 23681-2199

NASA/TM-2016-219154



Flat Plate Wake Velocity Statistics Obtained with Circular and Elliptic Trailing Edges

*Man Mohan Rai
Ames Research Center
Moffett Field, California*

National Aeronautics and
Space Administration

*Ames Research Center
Moffett Field, California 94035-1000*

August 2016

FLAT PLATE WAKE VELOCITY STATISTICS OBTAINED WITH CIRCULAR AND ELLIPTIC TRAILING EDGES

Man Mohan Rai¹

NASA Ames Research Center, Moffett Field, CA-94035

ABSTRACT

The near wake of a flat plate with circular and elliptic trailing edges is investigated with data from direct numerical simulations. The plate length and thickness are the same in both cases. The separating boundary layers are turbulent and statistically identical. Therefore the wake is symmetric in the two cases. The emphasis in this study is on a comparison of the wake-distributions of velocity components, normal intensity and fluctuating shear stress obtained in the two cases.

INTRODUCTION

The wake of the thin flat plate with a sharp trailing edge and turbulent boundary layers has been discussed in several articles, one of the earliest being that of Chevray & Kovaszny (1969). The ratio of the boundary layer momentum thickness to the trailing edge thickness of the plate (θ/D) is large (23.2) in their study ($D = 0.25\text{mm}$). Profiles of measured mean velocity and turbulent normal intensities and shear stress are provided. The boundary layers merge slowly to form the wake and large-scale vortex shedding is absent.

Ramaprian et al (1982), based on their own experimental data for a flat plate with a sharp trailing edge, and data from other studies, conclude that the wake only reaches an asymptotic state for $x/\theta > 350$ (θ is the momentum thickness of the *wake* in their study); they refer to the wake region upstream of this location as the “developing wake”. They suggest that the developing region be divided into the near wake ($x/\theta < 25$) and the intermediate wake ($25 < x/\theta < 350$). The near wake experiences the development of an inner wake and is influenced by the wall-layer of the upstream boundary layers. In the intermediate wake the effect of the upstream boundary layer diminishes and ultimately becomes insignificant.

Nakayama & Liu (1990) investigate the Reynolds number dependence of the wake centerline velocity profiles (normalized by the wall variables at the trailing edge), indicated by earlier experimental data. Their experiments (low Reynolds number, sharp trailing edge) show that indeed the profiles are Reynolds number dependent. They suggest that this is because of the effect of outer-layer eddies on the spreading of the inner wake.

Hayakawa & Iida (1992) obtained flat plate wake data with a sharp trailing edge (0.2mm) to better investigate the very near wake ($x^+ < 500$). The centerline velocity profile (x direction) was found to be similar to the velocity profile of the turbulent boundary layer (with counterparts to the viscous sub-layer, buffer layer and the log-law). The peak values in normal intensity and shear stress profiles in the cross-stream direction were found to first increase in the streamwise direction (x), from that obtained at the trailing edge, before diminishing further downstream. Based on space-time correlations, the authors attribute the initial increase in intensities and shear stress to an interaction between the wall turbulence from either side of the plate upon merger at the trailing edge and a change in orientation of longitudinal vortices. Of interest is the appearance of a broadband peak in centerline cross-stream velocity spectra, indicating quasi-periodicity (possibly due to vortices or wave-like motions).

¹ Senior Scientist for Computational Sciences, Exploration Technology Directorate

In addition to the experimental investigations mentioned above analytical solutions based on certain simplifying assumptions are provided by Albers (1980). In essence, the centerline velocity distribution in the x direction in the near wake can be approximated by a logarithmic relation similar in form to that obtained for the turbulent boundary layer upstream of the wake in these cases. A good comparison is obtained between experimental data and the wake 'log-law' in the near wake.

Thomas & Liu (2004) report on an experimental investigation of symmetric and asymmetric turbulent wakes behind a flat plate. The thickness of the plate is tapered down to 1.6 mm in the last 0.2 meters of the plate length. Hence, as in earlier flat plate wake experiments, little or no vortex shedding is expected. The asymmetric wake is obtained by introducing a semicircular bump on the lower side and a suction slot on the upper side. The net effect is a ratio of θ_L/θ_U of 2.5. Data are provided for adverse, favorable and zero pressure-gradient wakes.

In contrast to the thin plate with a sharp trailing edge, the thick plate with a blunt trailing edge (small θ/D case), exhibits vigorous vortex shedding. Unlike the case of the cylinder, the Reynolds number based on momentum thickness of the boundary layer just upstream of the trailing (Re_θ) and the Reynolds number defined using the thickness of the flat plate or the diameter of its trailing edge (Re_D), are independent parameters. A detailed computational investigation of the wake of the thick plate with a circular trailing edge and *turbulent separating boundary layers*, was initiated by Rai (2013, 2014 & 2015). This was accomplished with direct numerical simulations (DNS). The boundary layers as well as the wake were computed via DNS in these investigations. The separating boundary layers are fully turbulent well upstream of the trailing edge and are statistically identical. Thus the wake is symmetric in the mean.

The objective of the present investigation is to better understand the changes in the characteristics of the wake of a flat plate with turbulent separating boundary layers as the geometry of the trailing edge is modified. Two different trailing edges are used in this study, a semi-circle and a semi-ellipse (major to minor axis ratio of 4.0). The emphasis is on the time-averaged distributions of the velocity components, normal intensity and fluctuating shear stress. The data used in the present investigation are obtained from two direct numerical simulations of flat plate flow (constant plate thickness and length). The turbulent boundary layers and the wake are all computed via DNS as in the earlier investigations. Here we continue the analysis of the near wake of the flat plate initiated in Rai (2013, 2014 & 2015).

A BRIEF REVIEW OF THE FLAT PLATE WAKE RESEARCH PERFORMED TO DATE (RAI, 2013, 2014 & 2015)

A first effort at visualizing some of the important features of the near wake, such as the strength and structure of rib vortices in relation to the shed vortices, their evolution in time, the internal structure of shed vortices etc. are provided in Rai (2013). Some of the findings are as expected (rib vortices in the braid regions) while others such as the presence of intense elongated spanwise vortices instead of a single columnar vortex in the cores provide new understanding of the cores and braids and the interaction between them. Figure 1, showing contours of instantaneous spanwise velocity in a (x, y) plane is provided as an introduction to the flat plate wake. The shed vortices and the embedding of the turbulent vortices within the shed vortices are evident. The signature of the rib vortices within the braid region connecting two subsequent shed vortices (one of the shed vortices is shown with an arrow) can be discerned.

Figures 2a & 2b show perspective views of the wake region (up to $x/D = 7.0$). Figure 2a shows the full spanwise extent of the computational region. Two surfaces of constant streamwise vorticity (equal in magnitude), positive (red) and negative (green) are shown in this figure. Rib vortices are observed in the braid regions (arrow marks one of them); many of them are paired (positive & negative) and some are solitary. The core regions show the rib vortices wrapping around the cores. This is more clearly visible in Fig. 2b, which, for the sake of clarity, only shows only 25% of the spanwise extent of the computational domain. A surface of constant vorticity magnitude (streamwise and cross-stream components only $\Omega = (\Omega_x^2 + \Omega_y^2)^{1/2}$, magenta) and, a surface of constant pressure (yellow) are shown in Fig. 2b. The surface of

constant pressure shows the position of the cores. The elongated yellow segments associated with some of the rib vortices are indicative of a pressure minimum running along their length.

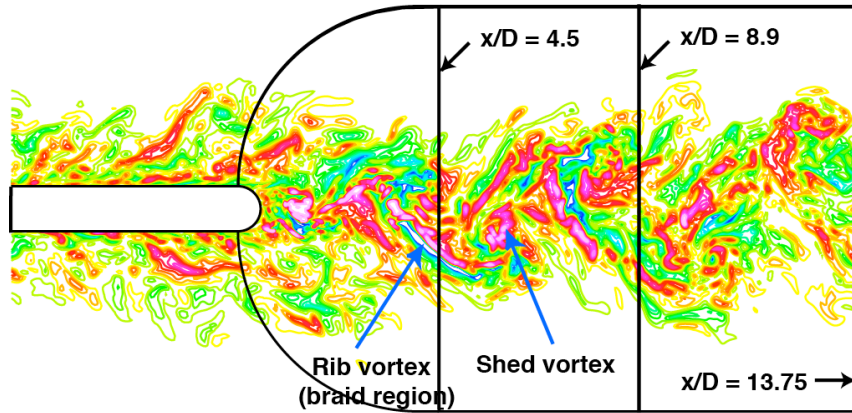


Fig. 1. Contours of instantaneous spanwise velocity in a (x, y) plane; red/magenta represent high/highest positive values, green/blue low/lowest negative values, yellow ≈ 0.0 .

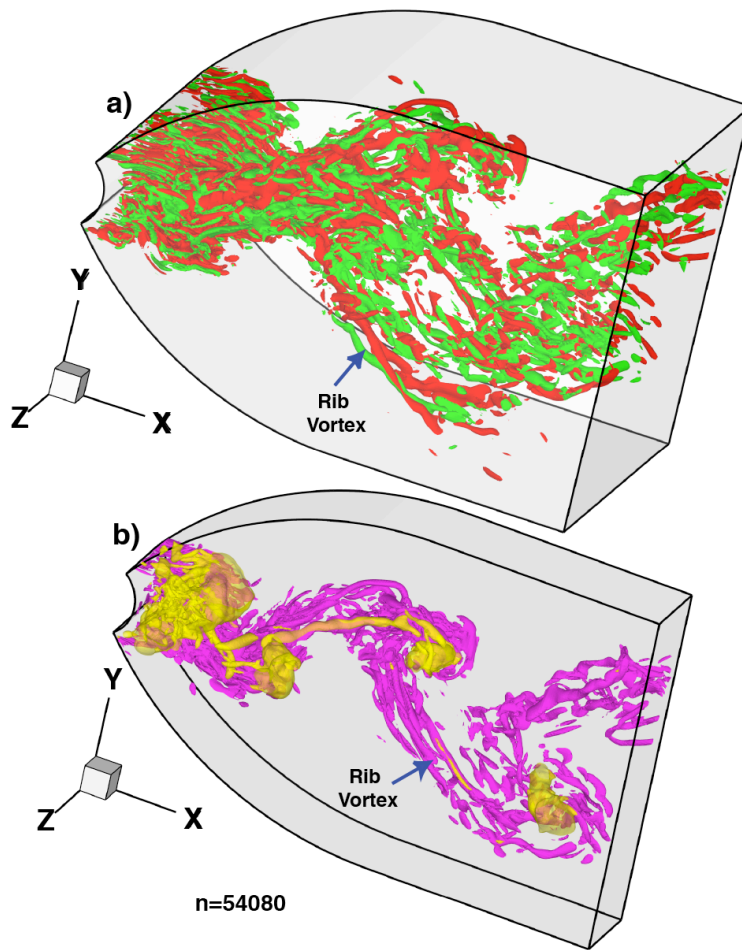


Figure 2. Perspective view of wake region (up to $x/D = 7.0$), a) surface of positive (red) and negative (green) streamwise vorticity, showing rib vortices (full span) and b) surface of constant vorticity magnitude (magenta) and pressure (yellow), showing rib and shed vortices (25% span only, Case A, Rai 2013).

To better illustrate the structure of the vortex core, Fig. 3a provides contours of instantaneous spanwise vorticity in an end-plane (y, z). This plane intersects the lower positive shed vortex indicated with an arrow in Fig. 1, at approximately its center. The fragmented nature of the core is evident. The level of fragmentation is expected since the vortices are formed by the roll-up of turbulent shear layers. It should be noted that the region $1.0 < z/D < 3.0, y/D > 0.0$ corresponds to the braid and not the shed vortex. The elongated positive vortices that comprise the core are evident ($y/D < 0.0$). Peak vorticity values are about 5 times as large as the peak phase-averaged spanwise vorticity at nearly the same x location ($5.7D$) as the end-plane. Interspersed among the positive vortices are regions of *negative vorticity*. They are weaker and in general do not have the characteristic shape of the positive vortices. Some of the negative vorticity is accumulated in the initial formation of the positive shed vortices when they are in close proximity to the turbulent shear layers from the opposing side.

Figure 3b shows pressure contours in the same plane and time instant as in Fig. 3a. The core as represented by the pressure does not show the level of fragmentation seen in Fig. 3a. It has been observed here that the pressure fields of closely spaced turbulent vortices merge into a single low-pressure region. The nearly circular pressure minima above and below the core in Fig. 3b are a cross-section of the rib vortices that have wrapped themselves around the core as in Fig. 2b.

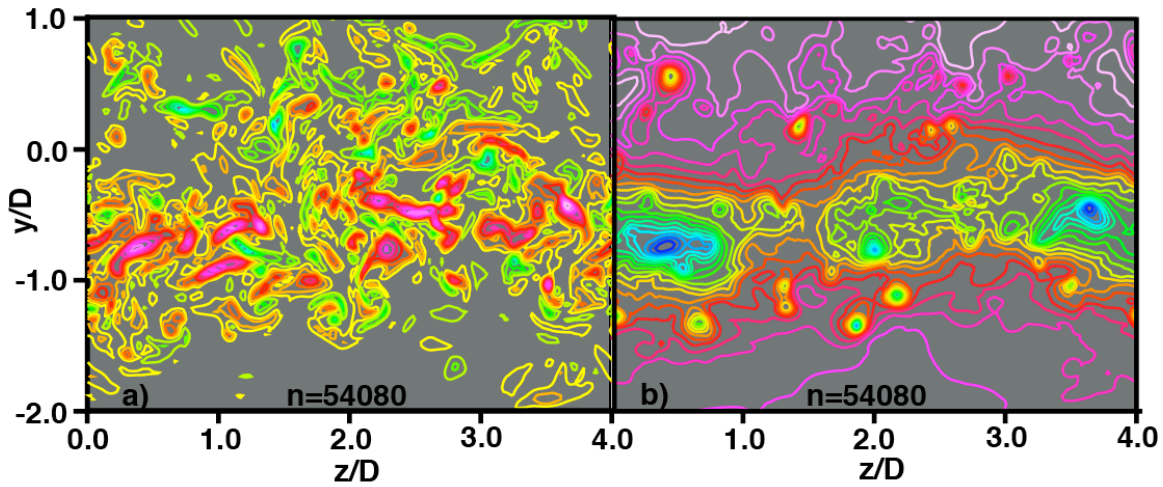


Figure 3. Contours of a) instantaneous spanwise vorticity; red/magenta represent high/highest positive values, green/blue low/lowest negative values, yellow ≈ 0.0 and b) instantaneous pressure, in the end plane (y, z) at $x/D = 5.7$, (Case A, Rai 2013).

The fluctuating density, pressure and velocity components in the flow field are assumed to contain a mean component, a periodic component at shedding frequency ω_{st} (and harmonics thereof), and a random turbulent component as in Reynolds & Hussain (1972). Thus a flow variable q is written as

$$q = \bar{q} + q' + q'' \quad (1)$$

where \bar{q} is the mean value, and q' and q'' are the random and periodic fluctuating components, respectively. The phase-averaged value $\langle q \rangle$ (average at constant phase) is given by

$$\langle q(\phi) \rangle = \bar{q} + q''(\phi) \quad (2)$$

where ϕ is the phase, $0.0 \leq \phi \leq 1.0$. The computed data are averaged in the z direction to obtain both the time-averages and phase-averages since the flow is homogeneous in this direction. A new event-based phase-averaging procedure is introduced in Rai (2013).

Distributions of the phase-averaged turbulent intensity and shear stress (random component) in the near wake are explored and compared with cylinder experimental data (Cantwell & Coles, 1983 & Hayakawa & Hussain, 1989) in Rai (2013). Wherever possible a physical explanation of the origin of the important features of the distributions, as well as one based on the distribution of the production term in the corresponding budget, is provided. Figure 4 shows distributions of the phase-averaged normal intensity and shear stress at one phase from Rai (2013). Phase-averaged pressure contours (magenta dashed lines) show the vortex core locations.

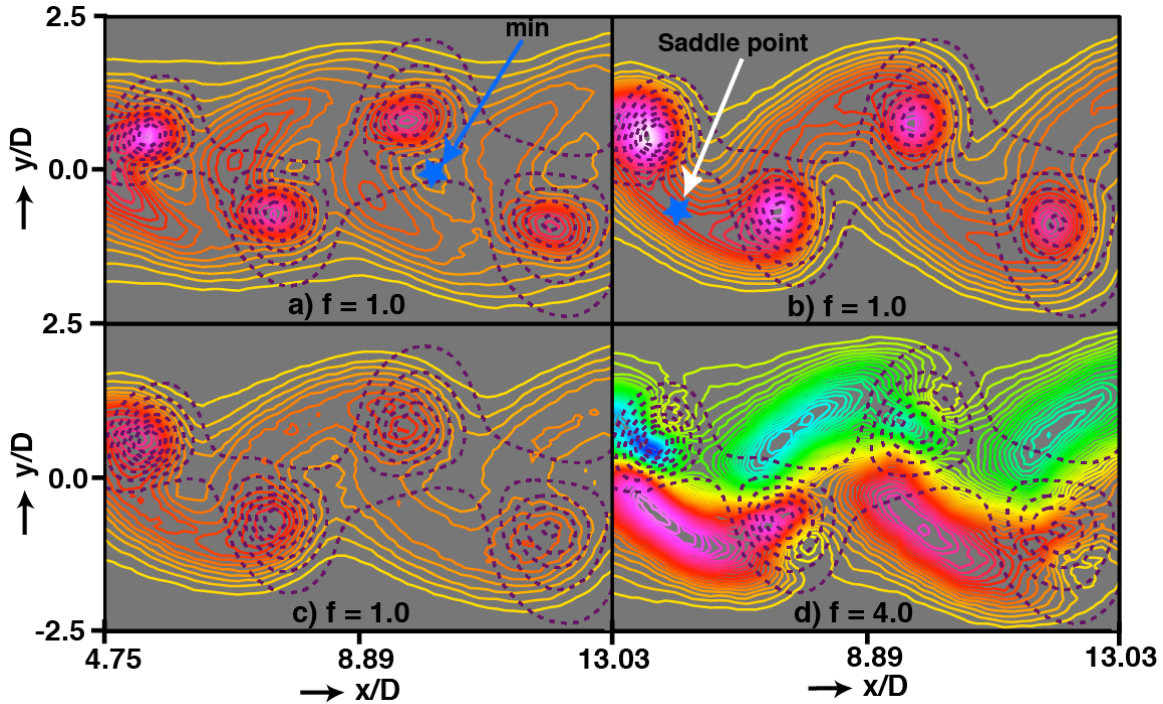


Figure 4. Contours of a) $\langle u'u' \rangle$, b) $\langle v'v' \rangle$, c) $\langle w'w' \rangle$ and d) $\langle u'v' \rangle$, and, $\langle p \rangle$ ($\phi = 0.0$); red/magenta represent high/highest positive values, green/blue low/lowest negative values, yellow ≈ 0.0 (Case A, Rai 2013).

Earlier research had primarily dealt with rib vortices as they occur in the braid regions and the amplification of the streamwise and transverse vorticity associated with them by vortex stretching as a result of the phase-averaged strain rate. In Rai (2013), it is found, that on average the stretching of rib vortices via the phase-averaged strain rate produces significantly less turbulent vorticity than that produced by turbulent stretching both in the braid regions and in the cores. In particular the data show the importance of turbulent stretching in sustaining fluctuations in the spanwise component of vorticity.

In Rai (2014) the emphasis is on the stability of the detached shear layers, rib-vortex induced reverse flow, and phase-averaged distributions of the random component of normal intensities and shear stress and the production term in the corresponding budgets in the very near wake ($x/D < 3.0$). It was determined that, as in the case of the cylinder with laminar separating boundary layers, the flat plate wake also exhibits shear layer instability followed by the formation of shear layer vortices that have a profound impact on the structure of the shear layer and the formation of the shed vortices. However, unlike the cylinder cases, here only a small fraction of the separated turbulent boundary layer participates in the initial formation of the shed vortices and, it is this fraction that is unstable. As in Rai (2010) (cylinder case), periods of shear layer instability correlated well with the interaction of the shear layer with recirculation region vortices, and quiescent periods showed little or no interaction between the two. This is a strong indicator that this interaction is an important contributor to initiation of the instability. Spectra of the time-varying velocity and pressure within the shear layers at $x/D = 0.5$ were obtained. Unlike the cylinder case with laminar separating boundary layers, the spectrum of streamwise velocity did not show

a broadband peak. This is because of the large velocity fluctuations that are already present in the detached shear layer at its inception (turbulent boundary layer). The pressure signal on the other hand showed a clear broadband peak with the characteristic shear layer frequency. Figure 5 shows contours of instantaneous spanwise vorticity. The shear layer vortices labeled A & B in the upper detached shear layer are evident; a newly formed shed vortex is highlighted with a rectangle. Figure 6 shows the spectrum of fluctuating pressure obtained at the locations marked H in Fig. 5. The sharp peak caused by vortex shedding, and the broadband peak caused by the shear layer vortices, are both visible.

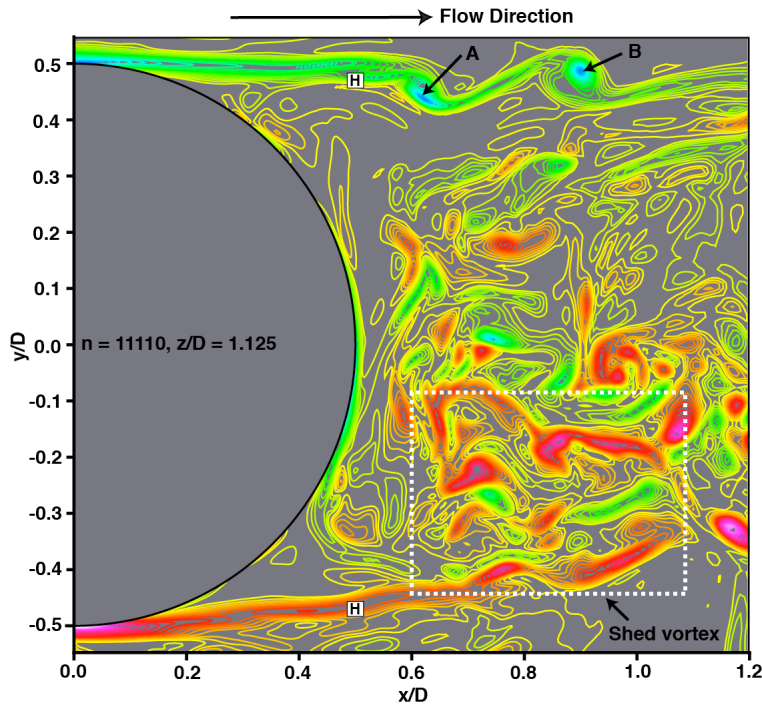


Figure 5. Contours of instantaneous spanwise vorticity at $T/T_p = 6.35$ (Case A, Rai 2014); red/magenta represent high/highest positive values, green/blue low/lowest negative values, yellow ≈ 0.0 .

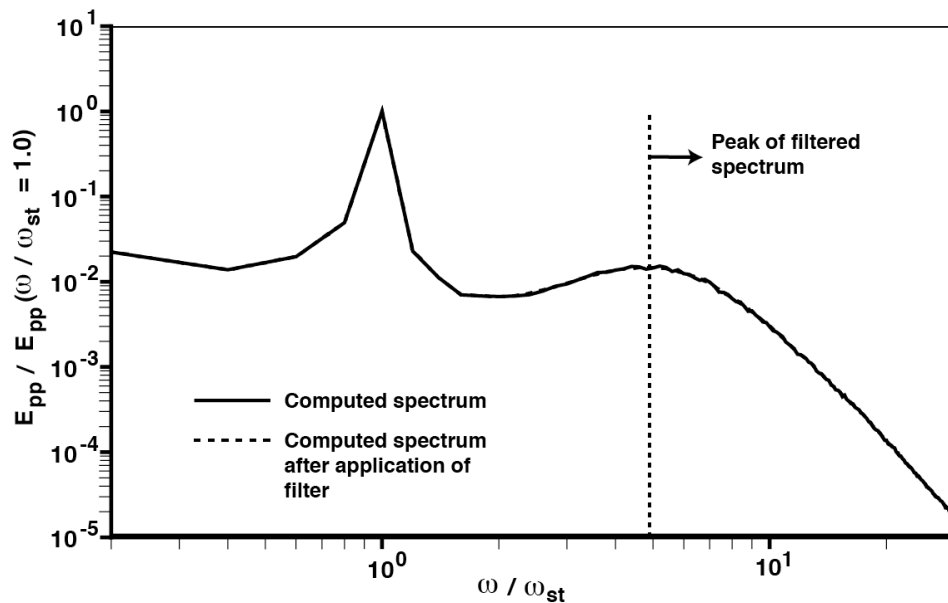


Figure 6. Spectrum of fluctuating pressure obtained within the detached shear layers (Case A, Rai 2014).

An examination of the distribution of instantaneous streamwise velocity in the wake center-plane (Rai, 2014) first led to the discovery of regions of isolated reverse flow that are disconnected from the main body of reverse flow in the trailing edge region. They are formed near the trailing edge and convect downstream. Figure 7 shows contours of instantaneous negative streamwise velocity at consecutive instants in time (T_p is shedding period) showing the formation of one such region of isolated reverse flow.

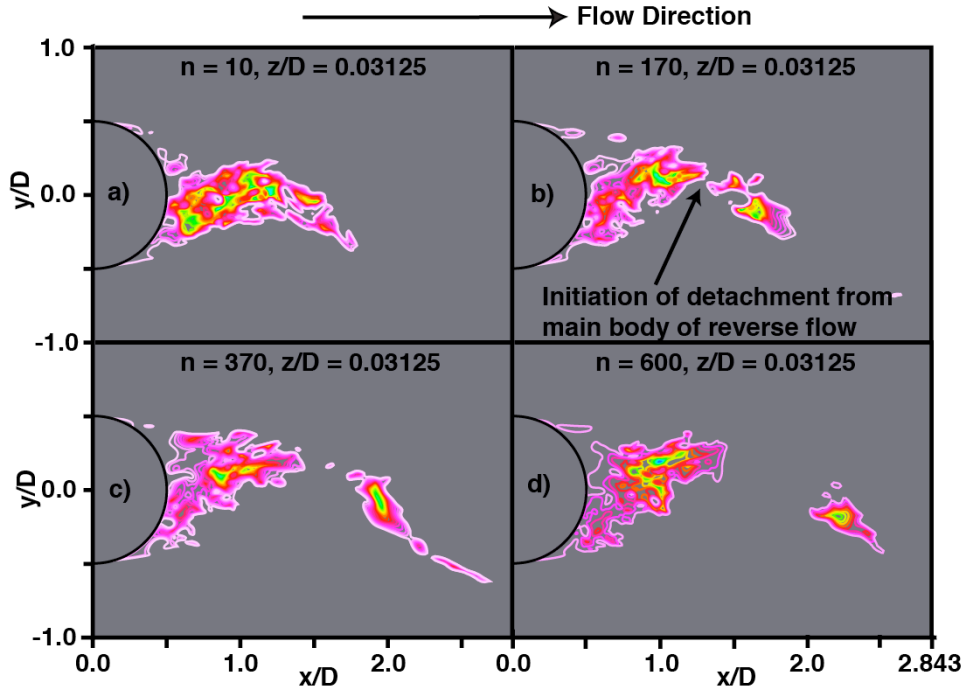


Figure 7. Contours in a (x, y) plane of instantaneous negative streamwise velocity at different instants in time showing the evolution of the rib-vortex induced region of reverse flow (Case A, Rai 2014); a) $T/T_p = 0.006$, b) $T/T_p = 0.097$, c) $T/T_p = 0.211$ & d) $T/T_p = 0.343$.

These regions are a result of powerful rib vortices that are formed in the high-strain-rate region that exists between the shed vortices in their initial state; they are quite energetic with streamwise velocities (negative) within them reaching 40% of the freestream velocity. They are accompanied by pressure minima and relatively high cross-stream vorticity levels and are observed as far downstream as $x/D = 4.0$. These reverse flow regions occur at multiple spanwise (z) locations within short periods (25% of shedding period); thus they appear along nearly constant time lines in a (t, z) plane at a given x location in the wake center-plane. Two such lines of reverse flow (each line corresponding to the passage of a shed vortex) are observed per shedding period. A spectral analysis of the z -averaged negative streamwise velocity shows a peak at twice the shedding frequency thus confirming the frequency of occurrence of these lines of multiple reverse flow regions. The passage of the shed vortices over a given x location reduces the local streamwise velocity near the center-plane thus creating favorable conditions for rib-vortex induced reverse flow. Since all such regions of isolated reverse flow investigated showed an associated rib vortex, it was concluded that the rib vortices were the causative agent. These regions eventually weaken and disappear; probable reasons being a re-orientation of the rib vortices (lowering of cross-stream vorticity) and the increase in streamwise velocity with increasing x .

In Rai (2015) the emphasis is on entrainment and the instability of the detached shear layers. It was observed in Rai (2014) that only a small fraction of the separating turbulent boundary layer participates in the initial roll-up into the shed vortex. A natural consequence is that for some distance downstream the wake with its shed vortices ingests fluid that was originally part of the turbulent boundary layer. The log-layer eddies are assimilated in this process and become a part of the shed vortices or the braids. A visualization of this process is provided in the article. A visualization of the effect of increasing

θ/D on assimilation/entrainment is also provided. It clearly shows that wakes with larger θ/D values continue to assimilate boundary layer fluid for longer (until a larger value of x/D); the important contributors to this effect are identified in the study. In addition, wake TKE profiles in the region away from the shed vortices and braids are very close to that of the upstream turbulent boundary layer (especially in the very near wake for the large θ/D cases). This again is a consequence of the fact that much of the turbulent boundary layer does not participate in the initial shed-vortex roll-up process.

A visualization of shear-layer instability events in a (t, z) plane in Rai (2015) showed that shear-layer vortex generation rates can vary as much as a factor of two from event to event. An analysis of velocity fluctuations in the upstream boundary layer indicated that high-speed streaks near the trailing edge result in higher rates of shear-layer vortex production.

As mentioned earlier, an important contributor to the shear-layer instability is the interaction between the shear layer and recirculation region vortices (Rai, 2014 & 2015). This of course raises the following question: Do interactions between the disturbances within the portion of the detached shear layer that rolls up into a shed vortex, and the log-layer eddies (travelling downstream), play a role in generating shear-layer vortices as well? The investigation of Rai (2015), shows that, like recirculation region vortices, log-layer eddies also generate shear-layer vortices. However, because the log-layer eddies travel downstream at a relatively high rate, they usually produce only one shear-layer vortex and continue to interact with it during their passage over the portion of the shear layer that rolls up into a shed vortex. Recirculation region vortices, on the other hand, remain in approximately the same position relative to the shear layer because of the much lower convection rates that they encounter. Thus they tend to produce a few shear-layer vortices that may be relatively powerful.

PLATE COMPUTATIONAL GRID, FLOW/GEOMETRY PARAMETERS AND NUMERICAL METHOD

The computational region for the flat plate DNSs is divided into two zones to facilitate grid generation and provide adequate grid resolution for the wake. Figure 8 shows the plate cross-section and the two zones that comprise the computational region. The three-dimensional zones and grids are obtained by uniformly spacing copies of these two-dimensional zones in the spanwise direction (z). The plate zone is bounded by four boundaries: the plate surface (excluding the trailing edge), an external boundary and, two zonal boundaries (top and bottom) that interface with the wake zone.

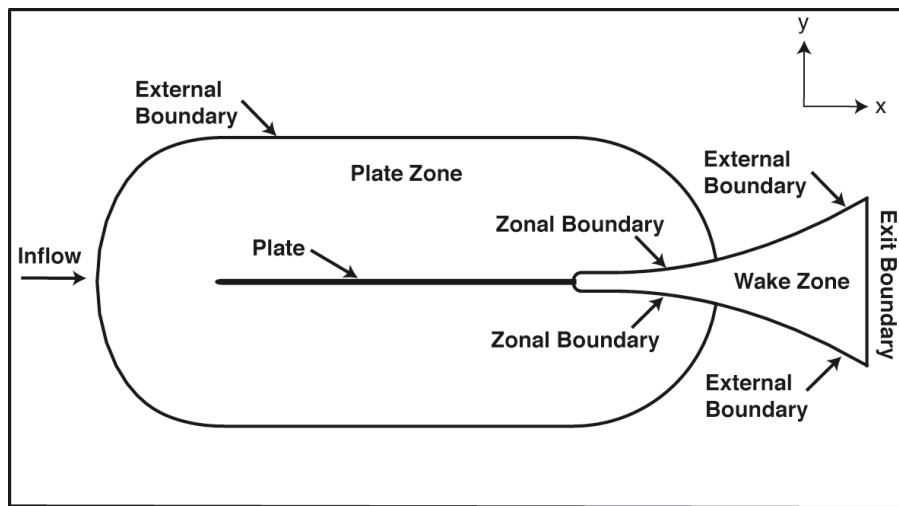


Figure 8. Midspan plate section and multiple zone discretization of the computational region (Rai 2013).

The plate zone captures the flow-field upstream of the trailing edge including the plate boundary layers. The leading edge of the plate is an ellipse. The wake zone is constructed to provide adequate grid resolution for the detached shear layers, the recirculation region and the wake. The boundaries of this zone include the circular trailing edge, the upper and lower boundaries and the exit boundary. Both the upper and lower boundaries consist of a zonal boundary segment that interfaces with the plate zone and a second segment that serves as an external boundary. Data from direct numerical simulations for two different trailing edges (circular, Case D and elliptic, major-to-minor axis ratio of 4.0, Case D^e) are used in this study. Of these, only Case D^e was computed as a part of the current investigation.

The placement of the various boundaries in relation to the plate surface in Cases A & D is provided in Rai (2013, 2014 & 2015). The vertical extent of the wake zone near the trailing edge, where its upper/lower boundaries are horizontal is large enough to completely contain the wake in all cases (as in Fig. 1). The spanwise extent of the region in Cases A & D is 4.0D. *Cases A & D of the present study are labeled as A & D in Rai (2015) as well.*

Figure 9 shows representative grids in the vicinity of the trailing edge in both zones for the circular trailing edge cases. These grids were generated with an algebraic grid generator. Both the plate and wake grids have the same spacing in the wall normal direction at the plate surface. The grid in the wake zone transitions from curvilinear near the trailing edge to rectangular downstream. In Cases A, D & D^e, downstream of $x/D \approx 13.5$, the wake grid coarsens gradually in the x direction. In addition to reducing the computational costs, this coarsening dissipates the wake to a degree that inviscid exit boundary conditions can be employed at the exit boundary of the wake zone.

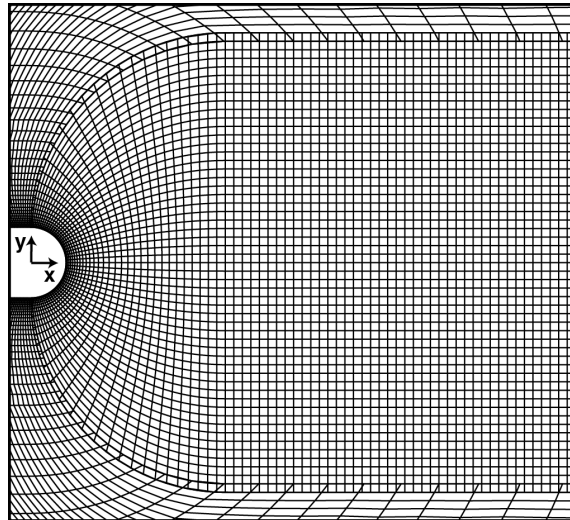


Figure 9. Representative grids in the plate and wake zones in the trailing edge region (Rai 2013).

The wake grid for Case A (reference case) was constructed with 741 grid points in the streamwise direction, 411 in the cross-stream direction and 256 in the spanwise direction (about 78×10^6 grid points). The resolution achieved along the centerline in the three spatial directions at $x/D = 10.0$ is approximately $\Delta x/\eta = 3.7$, $\Delta y/\eta = 2.2$ and $\Delta z/\eta = 2.1$ where η is the computed Kolmogorov length scale at the same location. The grid resolution in the plate grid in the x, y and z directions for this case is about 17.8, 0.84 and 6.6 wall units respectively, based on the wall shear velocity near the end of the plate. The resolution achieved in all the cases used here is similar.

The adequacy of the grid resolution and domain size used is demonstrated in Rai (2013 & 2014). A comparison of computed boundary layer turbulent intensities with experimental data is provided in Rai

(2013). The computations are performed at a Mach number of 0.2. The Reynolds number based on plate length L is the same in all cases (A, D & D^e), $Re_L = 1.25 \times 10^6$.

The primary goal in the current investigation is to study the effect of changing the geometry of the trailing edge from circular to elliptic on various characteristics of the wake. Accordingly, the thickness and length of the plate in Cases D & D^e are the same and so is the placement of the various boundaries (zonal boundaries and exit boundary of the wake zone, external boundary of the plate zone). In addition, the spanwise extent of the computational domain in the two cases (4.0D), the number of grid points used in the two zones and the wall normal grid resolution at the wall is the same in Cases D & D^e .

A high-order accurate upwind-biased method is used here to compute the flow over the plate as well as that in the wake. The convective terms are computed using sixth- and seventh-order upwind-biased finite differences, both with seventh-order dissipation terms. The viscous terms are computed with fourth-order central differences. The method is iterative-implicit in nature, multiple iterations are employed at each time-step to solve the nonlinear finite-difference equations arising from a fully implicit formulation; the method is second-order accurate in time. The boundaries that contain the computational grids can be classified as natural and zonal boundaries. The natural boundaries include the external boundary of the plate grid, the surface of the plate, the exit boundary of the wake grid, the segments of the upper and lower boundaries of the wake grid labeled as “external boundary” in Fig. 8, and, the boundaries in the z direction. The upstream segment of the upper boundary between the plate and wake grids is an example of the zonal boundaries used in the computation. Periodic boundary conditions are imposed on the boundaries in the z direction (homogeneity in z). No-slip/adiabatic wall conditions are used on the plate surface. Wall blowing/suction is implemented on a short segment on both the upper and lower surfaces of the plate to induce transition to turbulence. The boundary layer is turbulent well upstream of the trailing edge. The upper and lower transitional/turbulent boundary layers and the wake are all computed via DNS. The natural and zonal boundary conditions, and the high-order accurate upwind-biased finite-difference method used here are discussed in brief in Rai (2015) and in detail in the articles cited therein.

RESULTS

The data provided in the following figures were obtained during the data-sampling period (after the initial transients were eliminated). In the following contour plots the colors blue/green represent negative values (deep blue representing the lowest value) of the term/quantity being discussed. Orange, red and magenta represent positive values (magenta bordering on white representing the highest value). Shades of yellow represent values close to zero. *The specified minimum and maximum values and the numbers of contours in the subplots in the following figures are identical; the subplots within a given figure may be directly compared.* The distribution of time-averaged velocity statistics (also averaged in the z direction) in the wake region for Cases D and D^e are presented in this section. Intensities and fluctuating shear stress include the contributions from quasi-periodic shedding and the random component (Eq. 1).

The extent of the trailing edge (past $x/D = 0.0$) is different in the two cases. Here, unlike comparisons of cases with only circular trailing edges, downstream locations of minima/maxima etc. will (as necessary) be measured from the base (the point on the trailing edge that is furthest downstream) but, as before, normalized by the thickness of the plate (D). Accordingly we introduce the distance parameter $\xi = (x - x_b)/D$, where x_b represents the location of the base in the original coordinate system ($x_b/D = 0.5$ for Case D and $x_b/D = 2.0$ for Case D^e , see Fig. 9 for coordinate system origin).

Distributions of time-averaged velocity components

Figures 10a and 10b provide contours of time-averaged streamwise velocity \bar{u} for Cases D and D^e , respectively. The dashed white line corresponds to $\bar{u} = 0.0$; reverse flow is confined to the region between the base and this line. The separated region obtained in Case D is larger and separation occurs

sooner on the trailing edge. The zero contour line crosses the wake centerline at $\xi = 1.37$ & 0.89 for cases D and D^e , respectively. Peak reverse flow occurs at $\xi = 0.91$ & 0.45 for cases D and D^e , and the ratio of peak negative \bar{u} values in the two cases is 1.57 (D to D^e). Reverse flow in Case D^e is weaker.

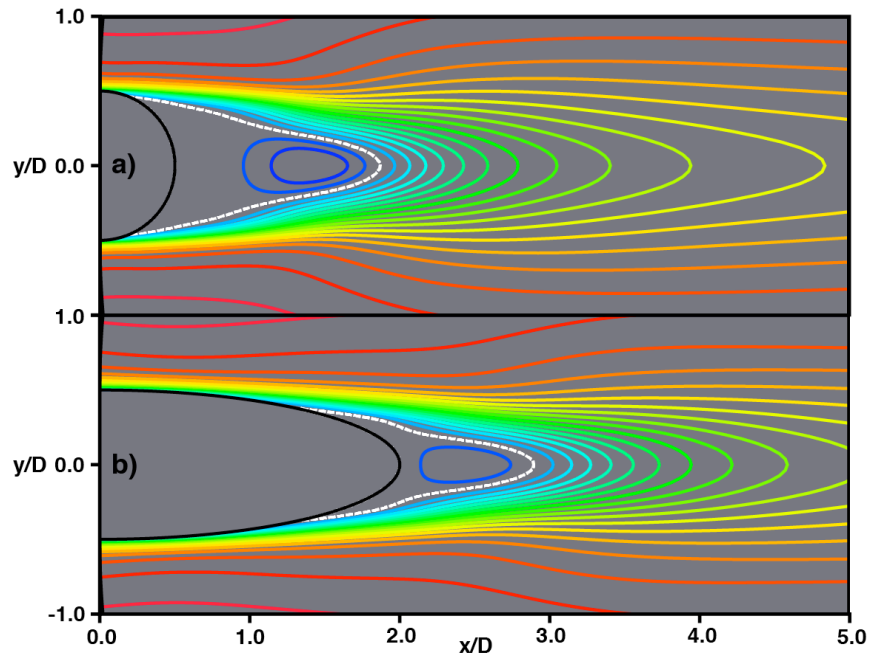


Fig. 10. Contours of \bar{u} , a) Case D and b) Case D^e .

Contours of time-averaged cross-stream velocity \bar{v} for Cases D and D^e are shown in Figs. 11a and 11b, respectively. A positive peak at $\xi = 0.57$ and a negative one at $\xi = 1.24$ in the upper half of the plane are evident in Fig. 11a.

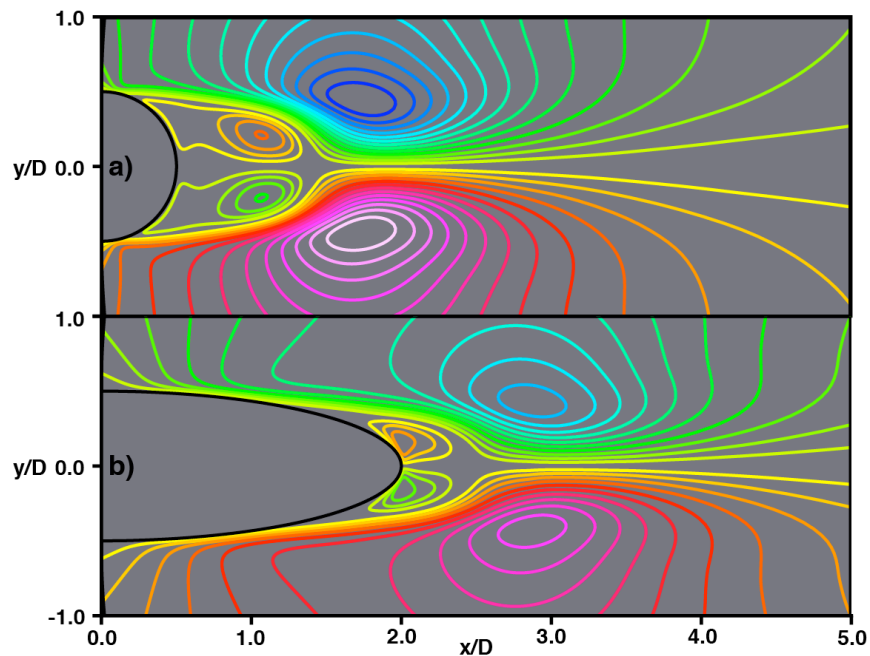


Fig. 11. Contours of \bar{v} , a) Case D and b) Case D^e .

These two peaks indicate the reverse flow in the base region and the induced, downward cross-stream flow, respectively; both caused by the negative shed vortices. The contours obtained in the lower half are a reflection of those seen in the upper half (with a sign change). The contours in Case D^e (Fig. 11b) are qualitatively similar but the cross-stream flow is weaker. The positive peak in the upper half of the plane occurs very close to the base and is associated with the reverse flow in this region. The negative peak, in relation to the positive peak, is quite distant from the base; it occurs at $\xi = 0.86$. However, relative to the negative peak obtained in Case D (Fig. 11a), it is closer to the base. The ratio of negative peak values is 1.32 (D to D^e).

Distributions of time-averaged normal intensity and fluctuating shear stress

Figures 12a and 12b show contours of time-averaged streamwise normal intensity for Cases D and D^e, respectively (including the contributions of both random and quasi-periodic fluctuations). While they are topologically similar, feature scales and locations are different. As expected both figures show non-zero levels in the turbulent separating boundary layers. Peaks in intensity, above and below the centerline, are observed in both cases. The peaks in Case D and D^e occur at $\xi = 1.29$ & 0.83, respectively. The ratio of peak values is 1.10 (D to D^e).

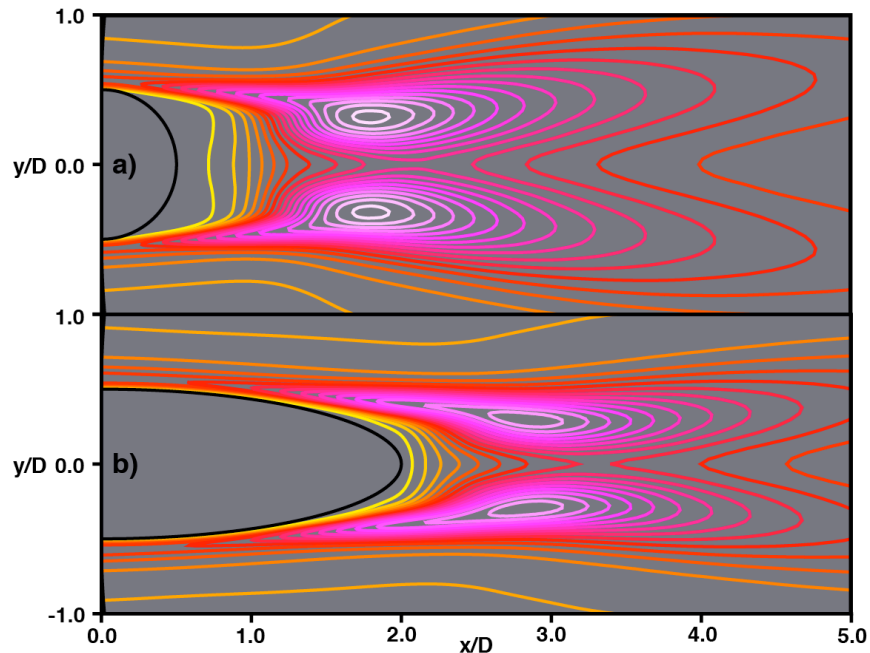


Fig. 12. Contours of time-averaged streamwise normal intensity (random & periodic),
a) Case D and b) Case D^e.

Figures 13a and 13b show contours of time-averaged cross-stream normal intensity for Cases D and D^e, respectively (including the contributions of both random and quasi-periodic fluctuations). Unlike in Fig. 12, both cases show a single maximum at the wake centerline. The peaks in Case D and D^e occur at $\xi = 1.59$ & 1.37, respectively. The ratio of peak values is 2.13 (D to D^e); the peak value obtained in Case D is significantly larger. The larger peak value is indicative of more powerful shed vortices in Case D.

Figure 14 shows the variation of streamwise and cross-stream normal intensities with ξ along the centerline for Cases D & D^e. While peak values of streamwise intensity are roughly the same (Case D shows a slightly larger peak), peak cross-stream intensity levels are substantially different. The peak

value in Case D (cross-stream component) is larger by a factor of 2.13 (as in Fig. 13) and, occurs slightly further away the base. The reason for the higher peak has been discussed earlier (stronger shed vortices in Case D). While the streamwise intensity level is also somewhat diminished in Case D^e; a significant portion of it is inherited from the boundary layer (approximately the same in the two cases).

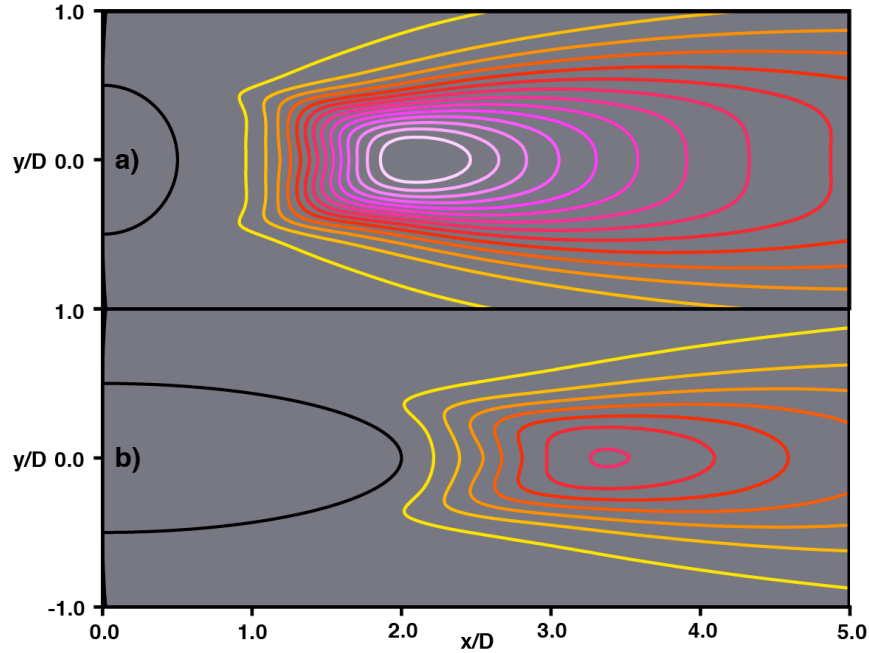


Fig. 13. Contours of time-averaged cross-stream normal intensity (random & periodic), a) Case D and b) Case D^e.

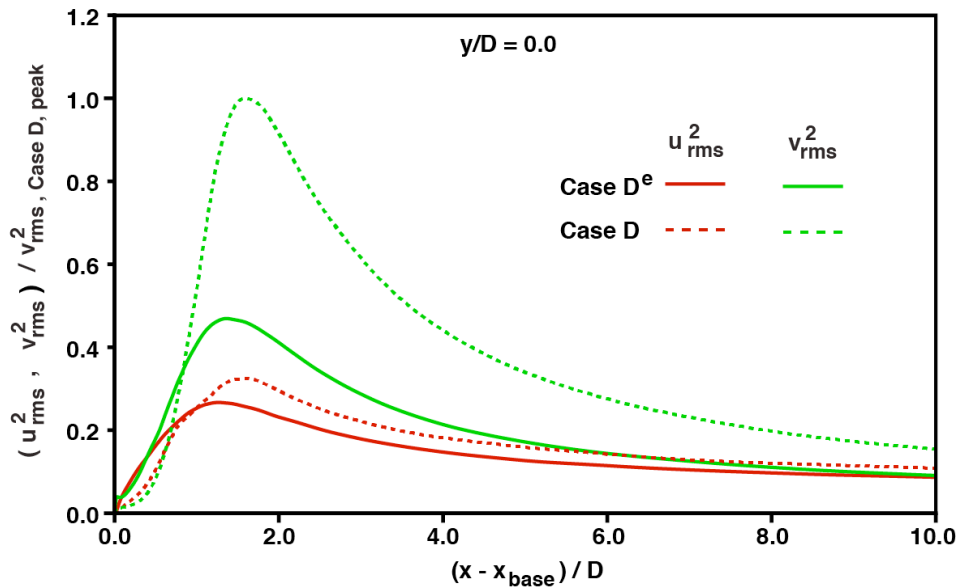


Fig. 14. Variation of streamwise and cross-stream intensities along the wake centerline for Cases D & D^e.

Contours of time-averaged fluctuating shear stress for Cases D and D^e are provided in Figs. 15a and 15b, respectively. The primary peak values (negative above, positive below) are seen in both cases. The peaks in Case D and D^e occur at $\xi = 1.50$ & 1.12 , respectively. The ratio of peak values is 1.50 (D to

D^e). In addition to the primary peaks in Fig. 15a, there exist much weaker secondary peaks (opposite in sign to the primary peaks) close to the base (see arrows). The secondary peaks are absent for Case D^e ; a plot with a large number of contours showed no indication of secondary peaks.

The origin of the secondary peaks is discussed at length in Rai (2011). It is shown there, in the context of Case A, that they are caused by the *periodic component* of fluctuating velocities resulting from the formation of the shed vortices. The two velocity components are positively/negatively correlated in the vicinity of the upper/lower secondary peak.

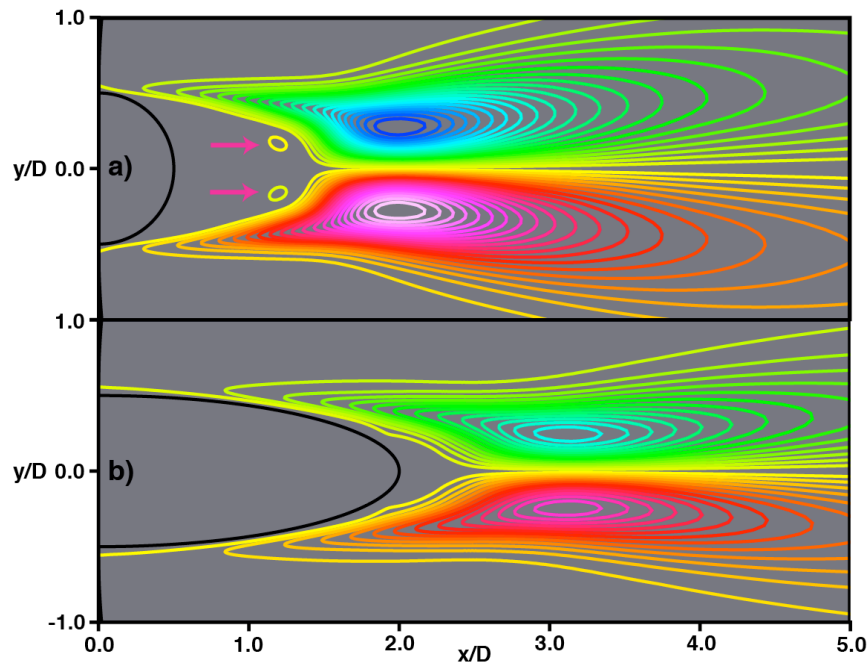


Fig. 15. Contours of time-averaged fluctuating shear stress (random & periodic),
a) Case D and b) Case D^e .

CONCLUDING REMARKS

The very near and near wake of flat plates with circular and elliptic trailing edges are investigated with data from direct numerical simulations. The plate length and thickness are the same in both cases. The upper/lower separating boundary layers in each case are turbulent and statistically identical. Therefore the wake is symmetric in the two cases. The emphasis in this study is on a comparison of the wake-distributions of velocity components, normal intensity and fluctuating shear stress in the two cases.

All of the wake-velocity distributions provided here indicate that the features observed in Case D are more intense than those obtained in Case D^e . This is true of peak negative \bar{u} , peak positive & negative \bar{v} , peak streamwise and cross-stream normal intensity and, peak fluctuating shear stress. In addition these peaks are located further downstream (in terms of ξ) *relative to the base* in Case D. These two attributes are indicative of stronger shed vortices that form further downstream of the base in Case D when compared to Case D^e . Thus, streamlining the trailing edge with an elliptic trailing edge (instead of using the traditional circular trailing edge) results in weaker shed vortices, a smaller region of separation and lower intensity levels. These are all attributes of interest not only from a fundamental flow physics perspective but also in turbine and compressor trailing edge design.

Interestingly, distributions of the components of velocity, turbulent intensity and shear stress are found to remain topologically quite similar with the change in trailing edge geometry (except for the secondary peaks in fluctuating shear stress); only the scales and locations of the various features such as maxima/minima are different.

REFERENCES

- ALBER, I. E. 1980 Turbulent wake of a thin flat plate. *AIAA Journal*, Vol. 18 (9), 1044.
- CANTWELL, B. & COLES, D. 1983 An experimental study of entrainment and transport in the turbulent near wake of a circular cylinder. *Journal of Fluid Mechanics*, Vol. 136, 321.
- CHEVRAY, R. & KOVAZNAY, L. S. G. 1969 Turbulence measurements in the wake of a thin flat plate. *AIAA Journal*, Vol. 7, 1641.
- HAYAKAWA, M. & HUSSAIN, F. 1989 Three-dimensionality of organized structures in a plane turbulent wake. *Journal of Fluid Mechanics*, Vol. 206, 375.
- HAYAKAWA, M. & IIDA, S. -I. 1992 Behavior of turbulence in the near wake of a flat plate at low Reynolds number. *Physics of Fluids A*, Vol. 4 (10) 2282.
- LIU, X., THOMAS, F. O. & NELSON, R. C. 2002 An experimental investigation of the turbulent planar wake in constant pressure gradient. *Physics of Fluids*, Vol. 14 (8), 2817.
- NAKAYAMA, A. & LIU, B. The turbulent near wake of a flat plate at low Reynolds number. *Journal of Fluid Mechanics*, Vol. 217, 93.
- RAI, M. M. 2010 A computational investigation of the instability of the detached shear layers in the wake of a circular cylinder. *Journal of Fluid Mechanics*, Volume 659, pp. 375-404.
- RAI, M. M. 2011 Flow Physics and Self-Similarity in the Turbulent Near Wake of a Flat Plate. Paper 2011-3575, 41st AIAA Fluid Dynamics Conference, Honolulu, Hawaii.
- RAI, M. M. 2013 Flow physics in the turbulent near wake of a flat plate. *Journal of Fluid Mechanics*, Volume 724, 704.
- RAI, M. M. 2014 Flow Phenomena in the very near wake of a flat plate with a circular trailing edge. *Journal of Fluid Mechanics*, Volume 756, 510.
- RAI, M. M. 2015 Detached shear-layer instability and entrainment in the wake of a flat plate with turbulent separating boundary layers. *Journal of Fluid Mechanics*, Volume 774, 5.
- RAMAPRIYAN, B. R., PATEL, V. C. & SASTRY, M. S. 1982 The symmetric turbulent wake of a flat plate. *AIAA Journal*, Vol. 20 (9), 1228.
- REYNOLDS, W. C. & HUSSAIN, A. K. M. F. 1972 The mechanics of an organized wave in turbulent shear flow. Part 3. Theoretical models and comparisons with experiments. *Journal of Fluid Mechanics*, Vol. 54, 263.